

First Collision Source in the IDT Discrete Ordinates Transport Code

Igor Zmijarevic, Daniele Sciannandrone

CEA-Saclay, DEN, DM2S, SERMA, F-91191 Gif-sur-Yvette, France
igor.zmijarevic, danielle.sciannandrone@cea.fr

Abstract - The first collision source calculation has recently been implemented in the IDT discrete ordinates nodal and short characteristics transport code. Several methods are developed and compared with the multigroup discrete ordinates transport code PARTISN and the continuous in energy Monte Carlo code TRIPOLI4[®]. The paper describes five different options: 1) a non-conservative scheme based on the tracking through the mesh centers, 2) a non-conservative averaging of mesh corner values, 3) cell based balance scheme with the surface averaged interface currents, 4) semi-analytic approach based on a conservative local-cell balance with numerical surface integration and 5) method of characteristics (MOC) based conservative scheme. The comparisons are performed on simple one group 3D test cases, one with a simple homogeneous geometry and another with very strong material heterogeneities. The detector responses are obtained for a 42-group 3D gamma shielding problem and compared. Results show that among the different options, the most robust are MOC, Mesh Center and Corner Average since they are positive, whereas schemes based on the Cell Balance may incur in negative solutions due to an inaccurate estimation of boundary currents. However, both Mesh Center and Corner Average have slow spatial convergence and may undergo conservation issues for coarse meshes. The MOC scheme, on the contrary, preserves global balance.

I. INTRODUCTION

IDT is a 1D/2D/3D discrete ordinates multigroup transport code that uses finite differences, nodal and short characteristics schemes in Cartesian geometry. It exists as a standalone mockup and as a part of APOLLO2 [3] and APOLLO3[®] [4] general purpose transport codes. It deals with homogeneous meshes [1] and heterogeneous ones that model the lattice pins cells in 2D and 3D with arbitrary number of concentric annuli [2]. A purely Cartesian mock-up has already been used for several source problem benchmark solutions [5, 6] with the volume distributed sources without first collision feature, albeit some situations were characterized by localized sources and weak scattering that essentially requires the use of the first collision source. Recently renewed interest in deterministic solutions of radiative transfer problems has motivated the development of a first collision source option in the IDT source problem solutions. The new developments will allow the use of IDT either for direct flux calculations, or in order to provide importance maps for Monte Carlo calculations. The standalone IDT is thus provided with the first collision source option, where several techniques have been investigated. The final version will include the first collision source from a set of point sources but also from the surface (internal interface) and volume distributed sources. The same ray-tracing technique used for the point source can also be used to improve the response of point detectors.

II. METHODOLOGY

In the first collision source method the solution of the transport equation with an isotropic point source of intensity q

at position \mathbf{r}_p

$$(\hat{\Omega} \cdot \nabla + \sigma)\psi(\mathbf{r}, \hat{\Omega}) = \sum_{\ell \geq 0} (2\ell + 1)\sigma_{st} \sum_{m=-\ell}^{m=\ell} Y_{\ell m}(\hat{\Omega}) \phi_{\ell m}(\mathbf{r}) + \frac{q_p}{4\pi} \delta(\mathbf{r} - \mathbf{r}_p) \quad (1)$$

is sought as the sum $\psi = \psi_u + \psi_c$, that is of the uncollided flux ψ_u plus the multiple collided flux ψ_c with the extra source defined as emission density from the first collision. The multigroup first collision source moments are

$$q_{\ell m}^g = \sum_{\ell m} \sigma_{st}^{g'g} \phi_{\ell m, u}^{g'} \quad (2)$$

The uncollided flux moments are computed as

$$\phi_{\ell m, u}^g(\mathbf{r}) = \int d\Omega Y_{\ell m}(\hat{\Omega}) \psi_u(\mathbf{r}, \hat{\Omega}), \quad (3)$$

$$\psi_u(\mathbf{r}, \hat{\Omega}) = \frac{q}{4\pi} \frac{e^{-\tau(\mathbf{r}, \mathbf{r}_p)}}{|\mathbf{r} - \mathbf{r}_p|^2} \delta\left(\hat{\Omega} - \frac{\mathbf{r} - \mathbf{r}_p}{|\mathbf{r} - \mathbf{r}_p|}\right), \quad (4)$$

where $\tau(\mathbf{r}, \mathbf{r}_p)$ is optical length between points \mathbf{r} and \mathbf{r}_p . This yields

$$\phi_{\ell m, u}(\mathbf{r}) = Y_{\ell m}(\hat{\Omega}_{\mathbf{r}_p \rightarrow \mathbf{r}}) \frac{q}{4\pi} \frac{e^{-\tau(\mathbf{r}, \mathbf{r}_p)}}{|\mathbf{r} - \mathbf{r}_p|^2}. \quad (5)$$

The above equation allows for a direct computation of the angular flux moments for a desired point \mathbf{r} using the ray tracing technique. Many implementations use the mesh cell centers as arrival point, assigning thus such a calculated value to the average flux within the cell. Others are based on cell vertices by taking their average values [12, 13, 14]. The codes based on the finite element approximation usually use the quadrature points set for the within cell numerical integration [10, 11]. These methods converge with the mesh refinement, but in general are not conservative, which means that one does not preserves the balance between emission rate and loss due to

collisions and leakage, so that the renormalization of the uncollided flux is necessary. Mesh refinement may be prohibitive especially in 3D, but the use of sub-meshing only for the purpose of uncollided flux calculation is possible, so that the detailed flux distribution on the sub-mesh is averaged over the problem mesh. Instead of sub-meshing a random set of trajectories can be used [9], where the selection is done in batches such that the variance of the flux can be computed.

Another approach is to use directly the local balance of each mesh cell [8], which for uncollided flux is obtained by integrating Eq. 1 without the scattering term over a cell volume V . The balance for the generic angular moment of order (ℓm) gives:

$$J_{\ell m}^{out,u} - J_{\ell m}^{in,u} + \sigma \phi_{\ell m,u} V = q \delta_{\ell m,00} \delta(\mathbf{r}_p \in V) \quad (6)$$

Where $\delta_{\ell m,00}$ means that only isotropic source is considered and $\delta(\mathbf{r}_p \in V)=1$ if the cell contains the point source and zero otherwise. The net current is expressed as contribution of surface integrated currents for each face of the 3D mesh cell. The problem of evaluating the flux moments is thus substituted by the problem of evaluating the interface currents. In this way, as the leakage on the outer boundaries is calculated in full consistency with the currents across the mesh cell interfaces, the global balance is automatically preserved. Slight additional complexity comes in the cases with vacuum cells. In this paper we investigate two ways of calculating the surface currents. The first is based on the direct computation of current components for cell vertices (i.e. the corresponding first angular moments, $\phi_{10}, \phi_{11}, \phi_{1,-1}$ for the corresponding cell faces) and taking the average value for the face current. The second is the one described in [8], here extended to Cartesian geometries.

III. FLUX MOMENTS CALCULATION

The code calculates the angular moments of uncollided flux directly using Eq. 5, which provides the information to calculate the average flux and surface currents for each mesh cell.

The basic options for the flux averaging in cell volume ϕ^v and on its surfaces ϕ^s are simply

$$\phi_{\ell m,u}^v = \frac{1}{8} \sum_{i=1}^8 \phi_{\ell m,u}^i, \quad \phi_{\ell m,u}^s = \frac{1}{4} \sum_{j=1}^4 \phi_{\ell m,u}^j, \quad (7)$$

where $\phi_{\ell m,u}^i$ and $\phi_{\ell m,u}^j$ are the values on cell vertices in 3D with j being the vertex index on a single cell face.

These values and additional calculations shown below allow us to formulate five different schemes:

Mesh Center This option uses the mesh-centered value of the uncollided flux as approximation for the average value. The total leakage is computed by using the cell-centered values of the x/y/z currents ($\phi_{\ell m}$, $m = -1, 0, 1$) of the outer boundary meshes.

Corner Average This option is based on a direct flux moment averaging by using the first expression in Eq. 7 whereas the second expression is used to evaluate the total leakage on outer boundaries.

Corner Balance This option is based on local cell balance where we use the second expression of Eq. 7 to compute the partial currents on cell interfaces. The same expression are used for the global leakage. Contrarily to other, this option is implemented in a way such that it is capable to compute the scalar flux only.

Semi-analytic This option is an adaptation to Cartesian meshes of the scheme proposed by Alcouffe et al. for R-Z geometries [8]. It is based on a local cell-balance together with an approximate surface integration of the currents.

MOC This option uses the method of characteristics to numerically integrate the flux moments in each computational mesh [7].

The details of the Semi-analytic method and of the MOC scheme are discussed in the following sections.

1. Semi-analytic method

The detailed analytical expression for the net currents in the scalar balance equation (Eq. 6), using the analytical expression of the uncollided flux (Eq. 4), is:

$$J_{\ell m}^{out,u} - J_{\ell m}^{in,u} = \sum_{\alpha} \int_{S_{\alpha}} d\mathbf{r} \hat{\Omega}_R \cdot \hat{\mathbf{n}}_{\alpha} Y_{\ell m}(\hat{\Omega}_R) \frac{e^{-\tau(\mathbf{r},\mathbf{r}_p)}}{|\mathbf{r} - \mathbf{r}_p|^2} \quad (8)$$

where the sum runs over the surfaces S_{α} delimiting the cell and having outgoing normal $\hat{\mathbf{n}}_{\alpha}$. The first approximation is to assume a constant value of the exponential attenuation for each surface which we compute as the average over the vertices of the face. Under this assumption we rewrite Eq. 8 as:

$$J_{out,u} - J_{in,u} = \sum_{\alpha} \Gamma_{\ell m}^{\alpha} \langle e^{-\tau(\mathbf{r},\mathbf{r}_p)} \rangle. \quad (9)$$

The expression and the calculation of $\Gamma_{\ell m}^{\alpha}$ is given in Sec. 3.

2. Method of characteristics

In the MOC option, a Cartesian mesh is built on the outer boundaries of the geometry domain and trajectories are tracked from the point source towards the mid-points of each boundary mesh. A solid angle $\Delta\hat{\Omega}_t$ is assigned to each trajectory t and a constant-flux approximation is done over the spherical surface defined by the distance R from the source. The flux over the surface is evaluated using Eq. 4 where the optical path is computed along the trajectory t .

For each intersection of a trajectory with the computational mesh we write a balance equation:

$$\sigma \psi_t = R_{in}^2 \psi_i (1 - \exp^{-\sigma l_t}), \quad (10)$$

with $l_t = R_{out} - R_{in}$ being the length of the intersection of the trajectory with the region, and ψ_t is the trajectory-integrated value of the angular flux.

The region-averaged values of the flux angular moments are determined by summing up all the contributions of the trajectories crossing the region:

$$\phi_{\ell m,u} \approx \frac{1}{\sigma V} \sum_t \Gamma_{\ell m}^t \psi_t. \quad (11)$$

In the last equation Γ_{lm}^t is the integration weight associated to each trajectory, which correspond to the integral of the Spherical Harmonics within the solid angle $\Delta\hat{\Omega}$ associated to the trajectory:

$$\Gamma_{lm}^t = \int_{\Delta\hat{\Omega}_t} d\hat{\Omega} Y_{lm}(\hat{\Omega}). \quad (12)$$

The volume V appearing in Eq. 11 is computed numerically by summing up the contribution of all trajectories and by using the weight for the zero-th moment (i.e., the solid angle):

$$\phi_{lm,u} \approx \sum_t \Gamma_{00}^t l_t \left(R_{out} R_{in} + \frac{l_t^2}{3} \right). \quad (13)$$

The Cartesian mesh used to define the trajectories does not need to coincide with the actual flux calculation mesh. At present, the basic option uses a constant mesh step. This, evidently, may be insufficient if the size of the flux mesh is smaller, such that no trajectory passes through a region. In order to remedy this situation, additional option allows to impose a minimum number of trajectories passing through the peripheral flux regions. This option may still miss some tiny regions in the domain interior and further improvements in adaptive tracking is necessary.

3. Quadrature formula

Both MOC and semi-analytic methods require the evaluation of the integral:

$$\Gamma_{lm}^\alpha = \int_{S_\alpha} dS \hat{\Omega}_R \cdot \hat{n}_\alpha \frac{Y_{lm}(\hat{\Omega}_R)}{R^2}, \quad (14)$$

where $\hat{\Omega}_R$ is the unit vector from the point source to the surface point \mathbf{r} , and R is the distance between the two points. An alternative form of the integral in Eq. 14 can be cast by introducing the change of variable $\mathbf{r} = \mathbf{r}_p + R\hat{\Omega}_R$ so that $dS |\hat{\Omega}_R \cdot \hat{n}_\alpha|$:

$$\Gamma_{lm}^\alpha = \int_\alpha d\hat{\Omega}_R Y_{lm}(\hat{\Omega}) sg(\hat{\Omega} \cdot \mathbf{n}), \quad (15)$$

where $sg(x)$ is the sign function of x , and the integral is for the trajectories emanating from the point source and intersecting the surface S_α . Under this form we can see that the coefficient Γ_{lm}^α corresponds to the integral of the Spherical Harmonic over the solid angle relative to the surface S_α .

The integration of Eq. 14 can be done analytically for a rectangular surface. In the particular case of the isotropic spherical harmonic, the resulting expression corresponds to the solid angle:

$$\Gamma_{00} = \tan^{-1} \frac{v_2 w_2}{u_0 r_{22}} + \tan^{-1} \frac{v_1 w_1}{u_0 r_{11}} - \tan^{-1} \frac{v_1 w_2}{u_0 r_{12}} - \tan^{-1} \frac{v_2 w_1}{u_0 r_{21}}, \quad (16)$$

with $r_{jk} = \sqrt{u_0^2 + v_j^2 + w_k^2}$. Here we have considered an orthogonal coordinate system uvw centered in the source, having u oriented along the normal to the surface, and such that $u = u_0$, $v = [v_1, v_2]$ and $w = [w_1, w_2]$ are the coordinates of the surface.

As an example, we also report here the primitive functions deriving from the integration over a surface oriented along the z direction of some of the first Spherical Harmonics:

$$\begin{aligned} \Gamma_{10} &= -\frac{z \tan^{-1} \left(\frac{y}{\sqrt{x^2+z^2}} \right)}{2 \sqrt{x^2+z^2}}, \\ \Gamma_{20} &= -\frac{xyz}{2(x^2+z^2)r}, \\ \Gamma_{30} &= -\frac{z \left((3x^2-2z^2)r^2 \tan^{-1} \left(\frac{y}{\sqrt{x^2+z^2}} \right) + 5x^2y \sqrt{x^2+z^2} \right)}{16(x^2+z^2)^{3/2} r^2}. \end{aligned}$$

For increasing orders, the complexity of these expressions increases so that it is difficult to cast them in a stable form for a correct numerical evaluation. For this reason, we choose to adopt a numerical approach and integrate Eq. 14 by partitioning the surface S_α in smaller rectangular sub-meshes and by using a rectangle-like quadrature formula:

$$\Gamma_{lm}^\alpha \approx \sum_n \Gamma_{00}^n Y_{lm}(\hat{\Omega}_n). \quad (17)$$

Here Γ_{00}^n is the isotropic coefficient associated to each sub-surface, whereas $\hat{\Omega}_n$ is the direction pointing to the sub-mesh centers. The integration is done by iterating on the number of sub-divisions until a given convergence criterion is met. Due to the oscillating nature of the Spherical Harmonics, the convergence rate of this strategy may be slow. However, for sufficiently small and distant surfaces, we found that one single sub-mesh is sufficient to provide an accurate solution. The iterative solution thus can be optionally deactivated to reduce the computational costs. The improvement of this integration strategy is a subject of future research and it is not deeply addressed in this work.

For the semi-analytic method we compute Γ coefficients for all the surfaces delimiting each mesh volume and for all anisotropy orders required to satisfy the region balance. Instead, for the MOC option, Γ coefficients are built only for a Cartesian mesh covering the geometry boundaries. It follows that for the semi-analytic method, the construction of the quadrature requires a larger number of operations.

4. Two dimensional case

In two dimensions the point source becomes a line source and the integration along the axial direction must be performed. This corresponds to the integration over the polar angle which results in higher order Bickley functions and different expressions for the analytical surface integrals. These are not considered in this paper.

IV. COMPARISONS

1. Two-zone cube

The first test case consists of a simple two zone geometry. An 11 cm cube with total cross section σ with a centered internal cube cavity of 1 cm containing the isotropic point source in its center. The five options which are referred here as

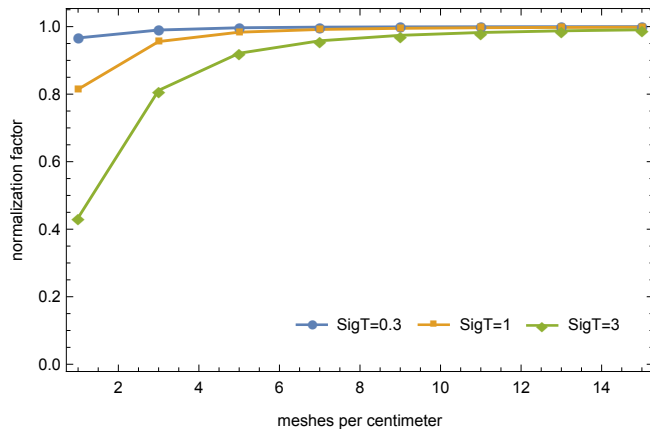


Fig. 1. Normalization factor for *Corner average* option per mesh size and different optical densities.

Mesh Center, Corner Average, Corner Balance, Semi-analytic and *MOC* scheme have been investigated for values of σ equal to 3, 1 and 0.3. The *Mesh Center* and *Corner Average* options are not conservatives, a problem which is customary addressed by introducing a normalization factor, f , defined such that:

$$f = \frac{Q - L}{R}, \quad (18)$$

where Q , L and R are respectively the total source intensity, the total leakages through the outer boundaries, and the total reaction rate calculated with the uncollided flux. This normalization factor can be considerably far from one in the case of optically large meshes, so we take this factor as a measure of the accuracy of the non conservative options. Figs. 1-2 show this factor for varying mesh size and for three values of the total cross section. It can be seen that the largest balance errors occur for optically large meshes. In order to further underline the issues deriving by using non-conservative schemes, we also show the total reaction rate in Figs. 2-2. It is clear that non-conservative schemes without renormalization may incur in a loss or an increase of the number of particles in the system. On the contrary, conservative schemes inherently preserve the globally-integrated reaction rates (provided a coherent estimation of internal and external interface currents). These values are those corresponding to the asymptotic values reached by the non-conservative schemes for a sufficiently fine mesh, and they are not showed in the figures.

Fig. 13 shows comparative plots of uncollided flux distributions in the horizontal mid-plane at the level of the point source calculated with three options. The mesh size used here is 15 meshes per centimeter and $\sigma = 3$. Strong oscillations occur around the source for the second option (*Balance*) that maybe due to the sensitive numerics involving the division by the square of distance and it needs further investigation. On the contrary, the *Semi-analytic* remains stable for the same mesh size and source distance.

2. Lead-concrete shielding problem

The second test case represent a mono-energetic point source next to a lead plate, which is 40 cm large and 5 cm

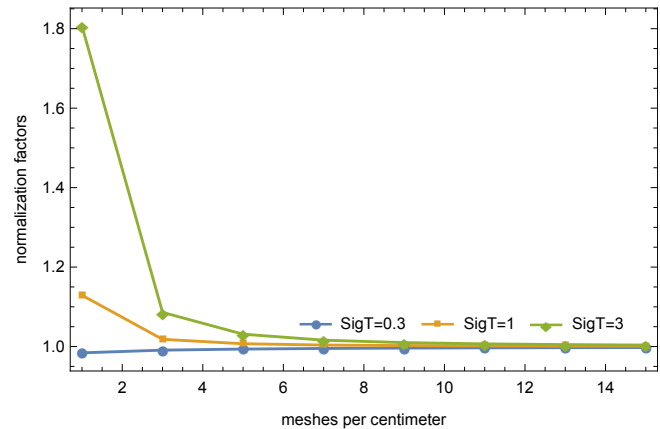


Fig. 2. Normalization factor for *Mesh center* option per mesh size and different optical densities.

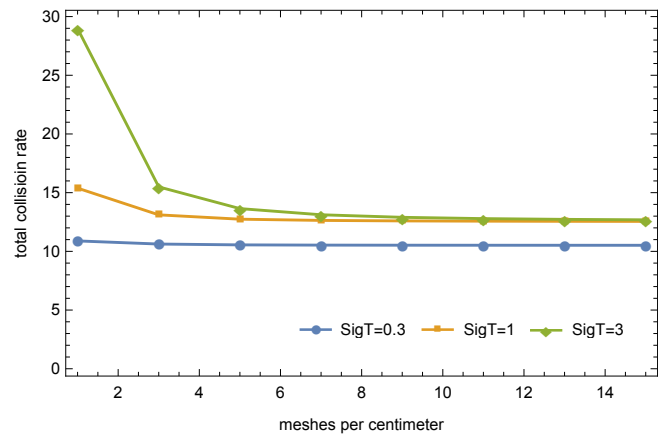


Fig. 3. Variation of total reaction rate with mesh size and different optical densities for *Corner average* option.

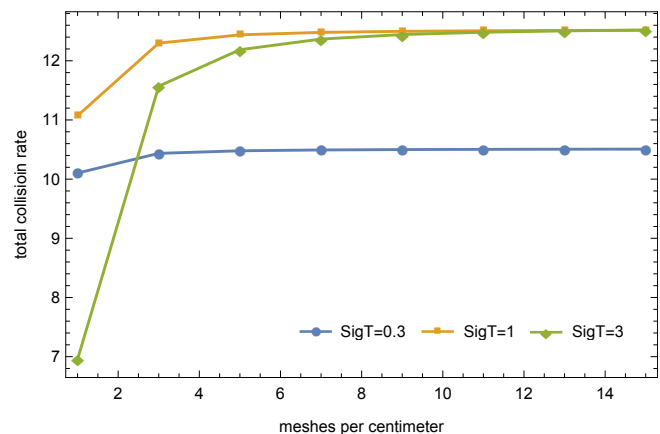


Fig. 4. Variation of total reaction rate with mesh size and different optical densities for *Mesh center* option.

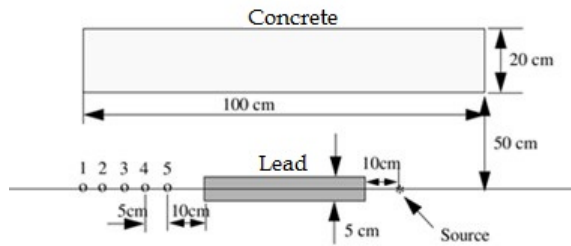


Fig. 5. Geometry of the Lead-concrete shielding problem.

thick as shown in Fig. 5. The concrete ceiling above is 20 cm thick. The length of 50 cm is adopted in the third dimension (y-axis), with the reflective boundary condition at the plane $y = 0$, where the source is situated. This test illustrates the application to the configurations with highly heterogeneous media.

Fig. 6 shows the normalized uncollided flux in the logarithmic scale along the symmetry plane where the source is positioned, obtained with *MOC* option, which provides a smooth solution. One may observe a linear decrease (exponential decay) of the flux along the lead shield. Contrarily to the first test case (simple cube) the non-conservative methods in this case give seemingly less sensitive solutions, which can be seen in Fig. 7. Strong material discontinuities produce the shadow effects which deteriorate the solution in the partially shadowed meshes resulting in negative flux values that are observed for *Corner Balance* and *Semi-analytic* options.

V. MULTIGROUP TEST CASE

We present a multigroup test case with the geometry shown in Fig. 8. The point source, which corresponds to a ^{60}Co gamma ray emitter, is positioned below a 20 cm thick concrete block, 2 m large and 1 m wide in the third dimension. Above the concrete, there is a series of aligned and equally spaced point detectors as shown in figure, for which the multigroup flux is calculated. The calculation is performed using the ZZ-KASHIL-E70, 42-group photon cross section library, provided by OCDE/NEA Data bank [15]. The results are compared with those of the TRIPOLI4[®] Monte Carlo code and also with the results of PARTISN [17] that uses the first collision source option. One must be aware that both PARTISN and IDT use the multigroup cross sections and are compared with continuous in energy Monte Carlo. The anisotropy of scattering is limited to P_3 Legendre expansion, which in this case is prone to the negative directional sources. In order to avoid the inconsistency in the treatment of negative values in PARTISN and IDT the option of the negative flux fix-up is turned off. The S_{30} discrete ordinates set of the Legendre-Chebyshev type with triangular arrangement is used in all calculations.

In the 42-group structure the ^{60}Co source emits in group 22 only. The results are also shown for the IDT without the first collision source option, where the point source is represented as a volume source within a small mesh of the size $(0.1 \times 0.1 \times 0.05 \text{ cm}^3)$. The relative errors of the flux values at the position of detectors for different codes and options are shown in Figs. 10 and 11. Four IDT options with first

collision source (FCS) are shown: with tracking through *Mesh centers*, *Semi-analytic* method, *Corner average* and *MOC*. Evidently, IDT without FCS is largely erroneous in the group 22 where the source emits. The other IDT options together with the PARTISN results follow each other closely in this group except for the detectors far from the source. A general underestimation of the flux in the far detectors is observed for all options, especially for the group 26.

The maximum contribution of the uncollided flux to the total flux in the group 22 at the level of detector plane is 71% (see Fig. 9). The consequence of the ray effect are clearly visible in Fig. 12 where the ratio of the fluxes calculated without and with the FCS option is shown. The group 26 in the figure shows the minimum far from the source, with a significant underestimation due to the insufficiently precise emission density which is a consequence of wrongly calculated flux in group 22.

VI. CONCLUSIONS

The standalone variant of the purely Cartesian IDT multi-dimensional nodal and characteristics discrete ordinates code is now operational with the first collision source capability. The angular emission from the point source is accounted by the ray tracing technique. Five different options were investigated. The first one is based on the tracking through the mesh centers, the second on the averaging of mesh corner values. Both are non-conservative schemes which require the renormalization in order to insure global particle balance. The three other are on the contrary inherently conservative. Among these are the cell based balance scheme with the surface averaged interface currents, and one with a semi-analytic approach based on local-cell balance using numerical surface integration. The first one manifests the instabilities due to the erroneous estimation of the interface currents, while the other remedies to this problem by providing more accurate integration weights. Nonetheless, for highly heterogeneous cases such scheme may be very sensitive as shown in the example. Finally the fifth option is based on the method of characteristics which appears to be an efficient alternative to all others, albeit it needs a careful choice of trajectory set in order to correctly treat very tiny regions. The detailed convergence studies will be done in further work.

The example of the 42-group shielding test problem shows that the use of FCS is of essential importance for a physically valid estimation of flux in deep penetration problems. The results also show that IDT with FCS is of equivalent accuracy as PARTISN transport code.

Although the development described here is related only to the point source, the volume distributed source may be treated using the sub-meshing feature. Further work will be oriented to the development of random ray-tracing and last collision flux for point detectors responses.

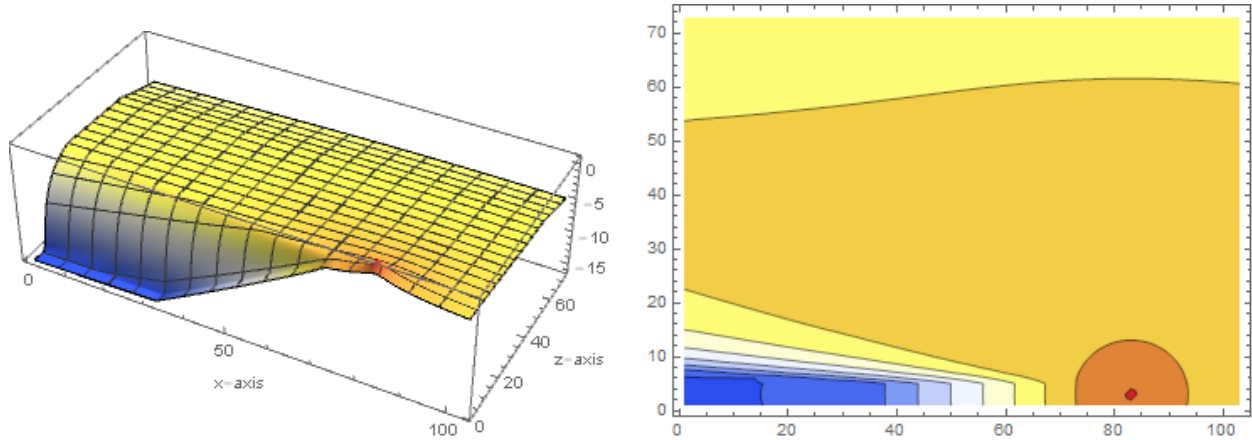


Fig. 6. 3D view (left) of the uncolided flux ($\log_{10} \phi$) in the plane containing the source of the lead-concrete problem using *MOC* option. 2D view of the same distribution is on the right.

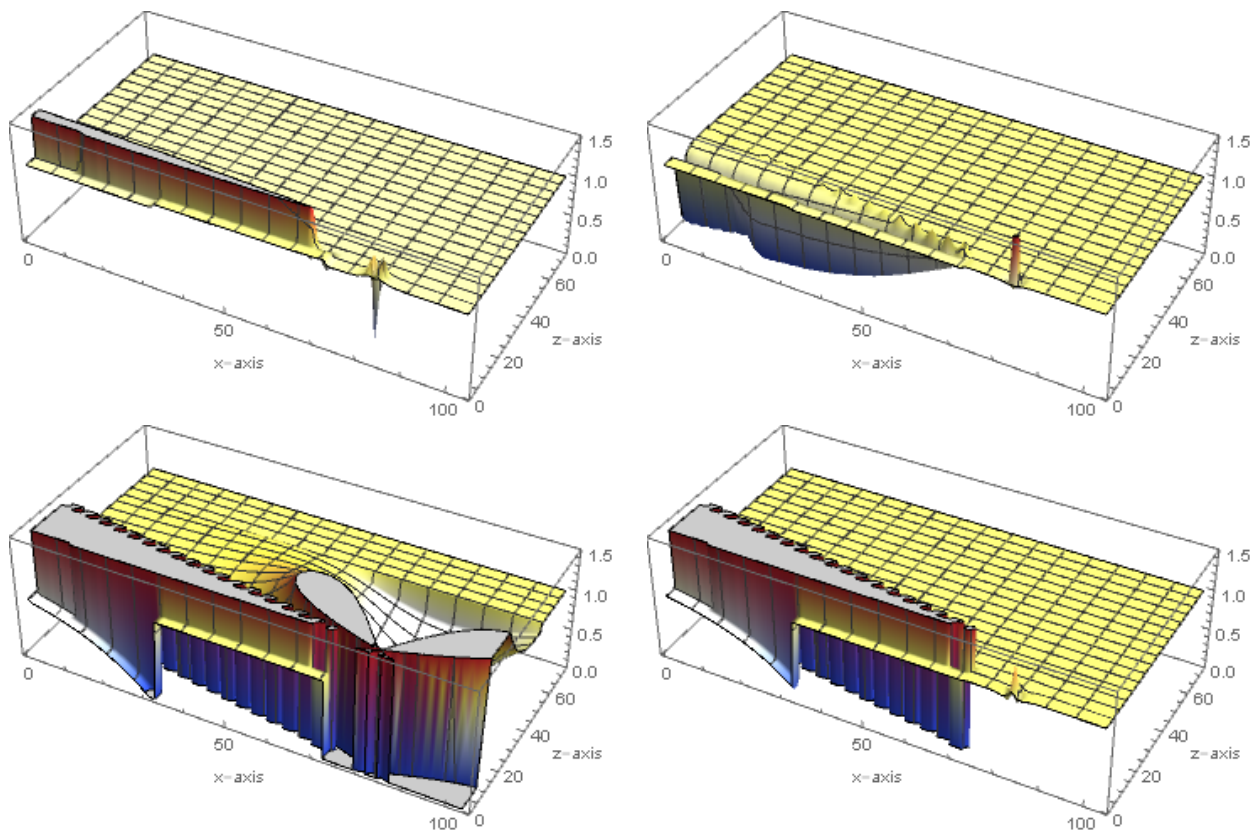


Fig. 7. Uncolided flux ratios. Four options relative to *MOC* solution: *Corner Average* (top-left), *Mesh Center* (top-right), *Corner Balance* (bottom left) and *Semi-analytic* (bottom-right). Grey surface is the limit of the truncated plot.

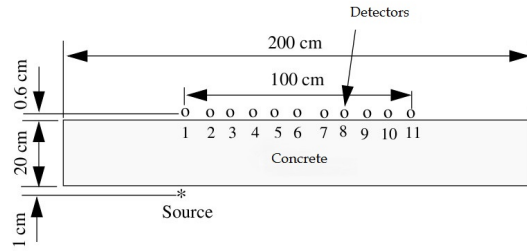


Fig. 8. Geometry of the multigroup test case.

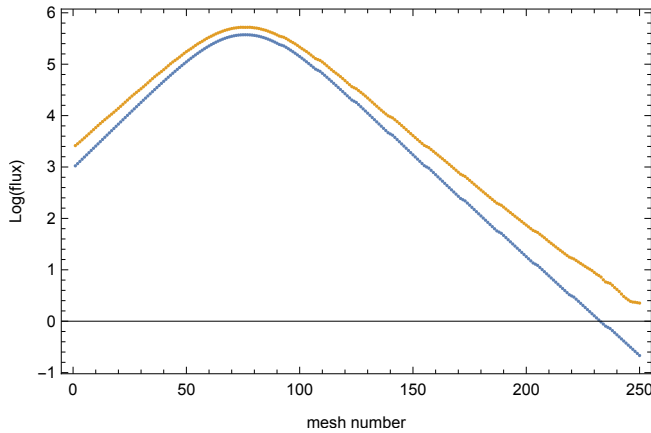


Fig. 9. Uncollided (blue) and total (orange) flux profiles in group 22 along the line of detectors.

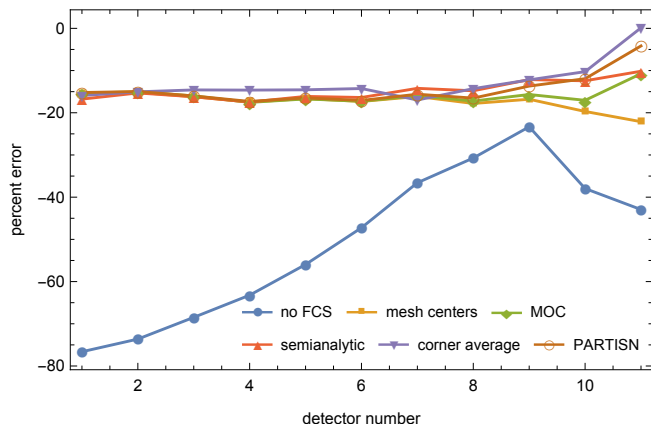


Fig. 10. Relative errors of the flux at the detector positions of the group 22, compared to Monte Carlo reference.

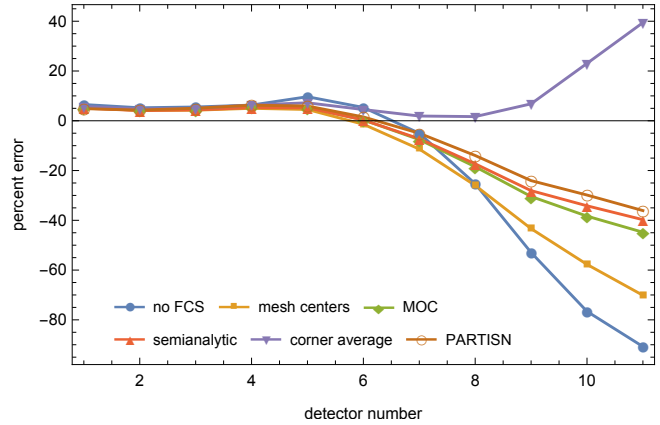


Fig. 11. Relative errors of the flux at the detector positions of the group 26, compared to Monte Carlo reference.

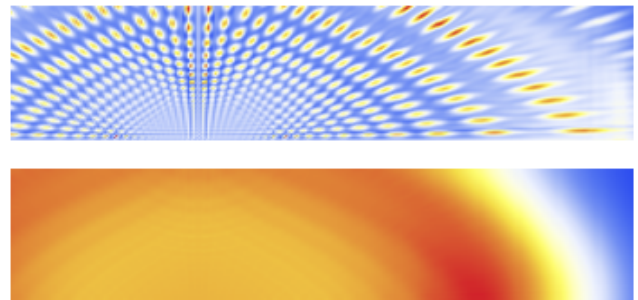


Fig. 12. Ratio of the fluxes calculated without FCS and the ones calculated using with FCS and MOC option for the groups 22 (top) and 26 (bottom). This is a top view on the plane passing through the detectors and parallel to the concrete surface

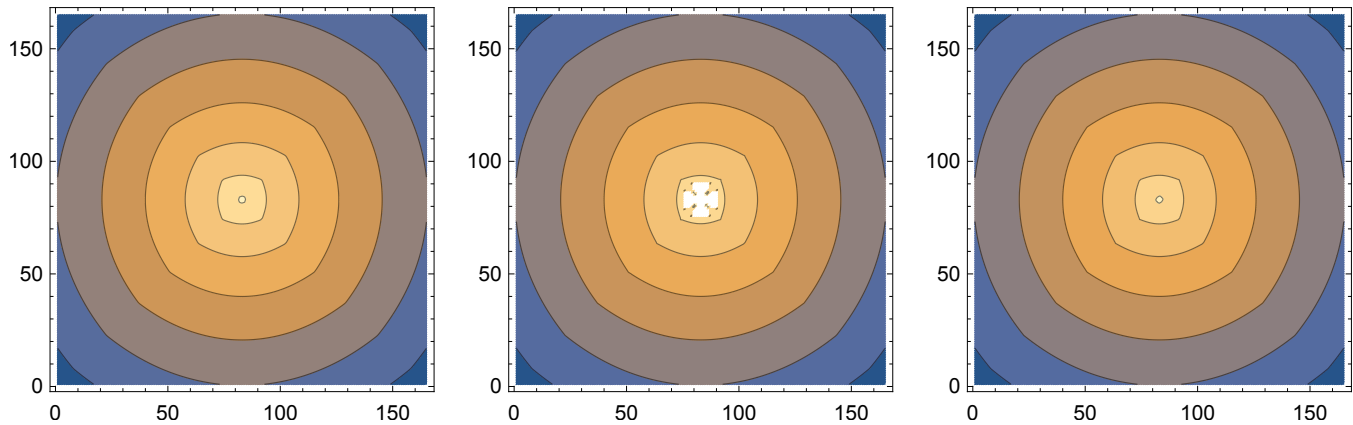


Fig. 13. Comparative plots of uncollided flux distributions in logarithmic scale in the horizontal plane containing the point source. The order of options is *Average*, *Balance* and *Semi-analytic*. The mesh size used is 15 meshes per centimeter and $\sigma = 3$.

REFERENCES

1. I. Zmijarevic, "Multidimensional Discrete Ordinates Nodal and Characteristics Methods for APOLLO2 Code," *Proc. Int. Conf. on Mathematics and Computation, Reactor Physics and Environmental Analysis in Nuclear Applications (M&C.99)*, Madrid, Spain, Sept. 27-30, 1999.
2. E. Masiello, R. Sanchez and I. Zmijarevic, "New Numerical Solution with the Method of Short Characteristics for 2-D Heterogeneous Cartesian Cells in the APOLLO2 Code: Numerical Analysis and Tests," *Nucl. Sci. Eng.* **161**, 257 (2009).
3. R. Sanchez, et al. "APOLLO2 year 2010." *Nucl. Eng. and Technology*, **42**, pp. 474-499 (2010).
4. D. Schneider et al., "APOLLO3: CEA/DEN Deterministic Multi-purpose Code for Reactor Physics Analysis", *PHYSOR 2016: Unifying Theory and Experiments in the 21st Century*, May 1-5, 2016, Sun Valley, Idaho, USA
5. Zmijarevic, I., Sanchez, R., "Deterministic solutions for 3D Kobayashi benchmarks." *Progress in Nuclear Energy*, vol. 39, no 2, pp. 207-221. 2001
6. I. Zmijarevic, "IDT solution to the 3D transport benchmark over a range in parameter space", *International Conference on the Physics of Reactors "Nuclear Power: A Sustainable Resource"*, Interlaken, Switzerland, September 14-19, 2008
7. D. Sciannandrone, S. Santandrea, and R. Sanchez, "Optimized tracking strategies for step MOC calculations in extruded 3D axial geometries," *Ann. Nucl. Energy*, 2016, vol. 87, pp. 49-60,
8. Alcouffe R. E., O'Dell R. D., Brinkley Jr F. W., "A First-Collision Source Method That Satisfies Discrete S_n Transport balance," *Nucl. Sci. Eng.*, 1990, vol 105 (2), p. 198
9. R. Alcouffe, "PARTISN Calculations of a 3D Radiation Transport Benchmark for Simple Geometries with Void Regions," *Nucl. Sci. Eng.*, 1990, vol 105 (2), p. 198
10. Wareing T. A, Morel J. E., Parsons D.K. "A First Collision Source Method for ATTILA." *Proc. ANS RPSD Top. Conf., Nashville. 1998 Topical Meeting on Radiation Protection and Shielding*, April 19-23, 1998, Nashville, TN
11. T. M. Evans, A. S. Stafford, R. N. Slaybaugh, and K. T. Clarno, "DENOV0: A New Three-Dimensional Parallel Discrete Ordinates Code in SCALE", *Nuclear Technology*, Vol. 171 p. 171-200 (AUG. 2010)
12. K. Kosako and C. Konno, "FNSUNCL3: First Collision Source Code for TORT", *Journal of Nuclear Science and Technology*, 37:sup1, 475-478 (March 2000)
13. F Masukawa, H Kadotani, Y Hoshiai, T. Amano, S Ishikawa, M R Sutton and N E Hertel, "GRTUNCL-3D: An Extension of the GRTUNCL Code to Compute R- θ -Z First Collision Source Moments", *Journal of Nuclear Science and Technology*, 37:sup1, 471-474 (March 2000)
14. Longfei Xu, Liangzhi Cao, Youqi Zheng, Hongchun Wu, "Development of a new parallel SN code for neutron-photon transport calculation in 3-D cylindrical geometry", *Progress in Nuclear Energy*, vol. 94, pp. 1-21, (January 2017)
15. "Nuclear Energy Agency - Databank Computer Program Services," 2016. [Online]. Available: <https://www.oecd-nea.org/dbprog/>. [Accessed: 26-Apr-2016]
16. E. Brun et al., "TRIPOLI4®: CEA, EDF and AREVA reference Monte Carlo code," *Ann. Nucl. Energy*, vol. 82, pp. 151-160, 2015.
17. R. Alcouffe, R. Baker, J. A. Dahl, S. Turner, and R. Ward, "PARTISN: A time-dependent parallel neutral particle transport code system," Los Alamos National Laboratory, LA-UR-08-07258, 2008.